International Journal of Thermofluids 23 (2024) 100721

Contents lists available at ScienceDirect

International Journal of Thermofluids

journal homepage: www.sciencedirect.com/journal/international-journal-of-thermofluids

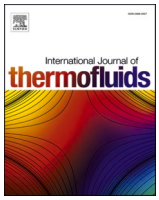

# Mapping electro-vortex flow patterns from tornado to inverted tornado in a hemispherical container

M. Abdi [a,b,c], E. Karimi-Sibaki [a,b], C. Sommitsch [c], H. Barati [d], M. Al-Nasser [a,b], M. Wu [b], I. Teplyakov [e], A. Kharicha [a,b,*]

[a] Christian Doppler Laboratory for Metallurgical Applications of Magnetohydrodynamics, Franz-Josef Street 18, 8700 Leoben, Austria
[b] Chair for Modeling and Simulation of Metallurgical Processes, Department of Metallurgy, Montanuniversität, Franz-Josef Street 18, 8700 Leoben, Austria
[c] Institute of Materials Science, Joining and Forming, Faculty of Mechanical Engineering and Economic Sciences, TU Graz, Kopernikusgasse 24/I, 8010 Graz, Austria
[d] K1-MET, Franz-Josef Street 18, 8700 Leoben, Austria
[e] Joint Institute for High Temperatures of Russian Academy of Sciences, 125412 Moscow, Russia

ARTICLE INFO

*Keywords:*
Electro-vortex flow (EVF)
Tornado
Cyclone
Magnetohydrodynamic (MHD)
Magnetic field
Swirl
Lorentz forces
Electric current intensity
Hemispherical container

ABSTRACT

This study aims to investigate the intricate interaction between fluid flow and magnetic fields, known as magnetohydrodynamic (MHD) phenomena, within a hemispherical container filled with conducting gallium–indium–tin (Ga-In-Sn) liquid. The primary objective is to explain the influence of the external magnetic field and electric current intensities on the flow structure. Novel insights into the emergence of Lorentz forces that drive the flow dynamics are pursued by varying these parameters. The motivation for this investigation is rooted in the desire to deepen our understanding and uncover new insights into magnetohydrodynamic (MHD) phenomena within a specific experimental setup. Specifically, we aim to understand how swirl velocity is generated and altered by fluctuations in magnetic field strength and electric current intensity within the system. Our investigation reveals a transformation in the flow pattern in a hemispherical pool as the magnetic field strength increases while maintaining a constant electric current intensity. Sequential transformations from a rope tornado to a tornado, cyclone, and finally an inverted tornado are observed, shedding light on the complex behavior of the system. On the other hand, under fixed external magnetic field conditions, it is observed that, as the electric current intensifies, the flow pattern evolves from a tornado to a rope tornado or from a cyclone to a tornado. Furthermore, once the electric current intensity exceeds a specific threshold, the flow pattern remains unchanged, providing valuable insights for process optimization and control. This study contributes to a deeper understanding of MHD phenomena and offers practical implications for optimizing processes such as electroslag remelting (ESR) and vacuum arc remelting (VAR) that involve a similar hemispherical pool of conductive liquid. The simulation results are validated against experimental measurements, ensuring the reliability and accuracy of our findings.

## 1. Introduction

When a non-uniform electric current travels through a liquid metal, it interacts with either a self-induced or an external magnetic field (The magnetic field can be generated by various sources, including the Earth's magnetic field [1], magnetic fields induced by current leads [2], and those produced by mixing devices [3].), resulting in the creation of an electromagnetic force [4]. Understanding this interaction, known as magnetohydrodynamic (MHD), provides insight into a variety of industrial processes, such as electroslag remelting (ESR) [5–8], vacuum arc remelting (VAR) [9–12], liquid metal batteries [13–16], and aluminum reduction cells [17–19].

For instance, Ranawade [20] introduces an MHD model incorporating electro-vortex flow (EVF) to simulate fluid behavior in liquid metal batteries (LMBs). The model predicts significant impacts on various flow phenomena, including EVF, thermal buoyancy, and solutal buoyancy on LMB performance. Furthermore, numerous studies have investigated Li‖Bi cell systems, particularly focusing on fluid dynamic phenomena. Various authors have developed three-dimensional models to analyze mass-transport [21,22].

* Corresponding author at: Christian Doppler Laboratory for Metallurgical Applications of Magnetohydrodynamics, Franz-Josef Street 18, 8700 Leoben, Austria.
*E-mail addresses:* mehran.abdi@unileoben.ac.at (M. Abdi), abdellah.kharicha@unileoben.ac.at (A. Kharicha).

https://doi.org/10.1016/j.ijft.2024.100721

Available online 12 June 2024

Understanding the MHD flow arising from the interaction between fluid flow and the magnetic field is essential, particularly in a hemispherical container. For example, in processes like Vacuum Arc Remelting (VAR), the molten pool forms a hemisphere due to cooling from the surroundings and solidification in the ingot [9–11,23]. The flow structures inside the hemisphere influence critical parameters such as the melting duration of the metal and the temperature distribution in the bath. Additionally, they affect the crystallization front [24–26], as well as the duration and quality of metal mixing [27]. In ESR, for example, a slight increase in the magnetic field causes stationary zones in the domain and overheats the metal bath [28].

Since this structure is sensitive to external axial magnetic fields and the intensity of the electric current, controlling the flow with the aid of these parameters is a natural solution that should be utilized with caution. Vinogradov [29], introduces a novel method for calculating magnetic fields in current-carrying media, utilizing unstructured grids and NVIDIA CUDA technology for accelerated computations, without prior knowledge of the computational domain's shape. Frick et al. [30] extensively investigated flow within a cylinder under the influence of an external axial magnetic field. The external magnetic field also plays a crucial role in EVF. For example, the application of a strong external axial magnetic field promotes the flow, inducing a secondary electric current [31]. Zhilin et al. [32] observed a horizontal swirling of EVF and proposed that such swirling in the liquid metal could be induced by external magnetic fields, similar to the magnetic field of the earth. The effect of the external magnetic field on azimuthal velocity, axial velocity, and kinetic energy was examined. The strength of the external magnetic field can either increase or decrease the intensity of the flow [28].

Modeling and experimental attempts were made to investigate the effect of electric current intensity on the flow structure within the hemisphere. Shercliff [33] studied flow patterns considering an electric current source and proposed an analytical solution for fluid motion. Malyshev et al. [34] performed numerical research on the Electro-Vortex Flow (EVF) with low electrical current using the Stokes approximation to calculated the velocity and pressure fields. The surface deformation below the electrode, in terms of depth, and the reasons for arc development around the electrode tip using different electric current intensities were explored numerically [35]. Teplyakov et al. [36] constructed an experimental setup to study the influence of electric current on the flow structure. They investigated the variation of EVF velocity as a consequence of current intensity within the hemisphere.

Vinogradov et al. [37] attempted to measure the velocity with the help of an experimental setup, as shown in Fig. 1(a). They reported a hydrodynamic self-oscillation, possibly arising from the interaction of two opposite vortices. However, experimental analyses alone may not suffice to fully understand this phenomenon. Measuring the velocity at a single point may not provide a comprehensive overview of the flow structure. Additionally, the accuracy of measurements depends on the limitations or resolution of the measuring instrument. This study presents a novel investigation into the behavior of conductive flow within a hemispherical container, a geometry that has received limited attention in prior research. The present study utilizes a model analogous to that used by Kharicha et al. [38], who investigated the behavior of a conductive fluid enclosed within a cylindrical vessel with a planar electrode.

The aim of this study is to delve into fundamental questions surrounding the influence of varying external magnetic fields and electric currents on flow structures within hemispherical containers. Key inquiries driving this investigation include: How do varying external magnetic fields influence the emergence and evolution of distinct flow patterns within the hemispherical container? What role does electric current intensity play in modulating the behavior of magnetohydrodynamic (MHD) phenomena within the experimental setup? Additionally, the research seeks to explore how the understanding of flow structures under different magnetic fields and electric current intensities can contribute to the optimization of industrial processes such as Electroslag Remelting (ESR) and Vacuum Arc Remelting (VAR). Furthermore, consideration is given to the limitations of current simulation approaches in accurately representing three-dimensional flow dynamics, with a focus on addressing these challenges to propel advancements in the field of MHD research.

## 2. Modeling

The experimental setup, shown in Fig. 1(a), was crafted to enable a thorough investigation into the behavior of an In-Ga-Sn eutectic alloy under controlled conditions. Fig. 1(b) offers a detailed perspective of the 3D axisymmetric cross-section, revealing the intricate regions and boundaries within the simulation domain. Central to this setup was a hollow copper hemispherical container acting as the crucible, providing a stable environment for housing the alloy. With a diameter of 188 mm, this container facilitated the execution of experiments on the alloy. Accompanying the copper crucible was a smaller counterpart, serving as the electrode. Shaped as a convex hemisphere with a diameter of 5 mm, it was submerged into the alloy to a depth of 2.5 mm. The flow of electric current density initiated at the electrode, traversing through the conductive liquid medium to ultimately reach the crucible. Power to the setup was delivered by a sophisticated current source employing a Larionov rectifier scheme, ensuring a consistent current flow with

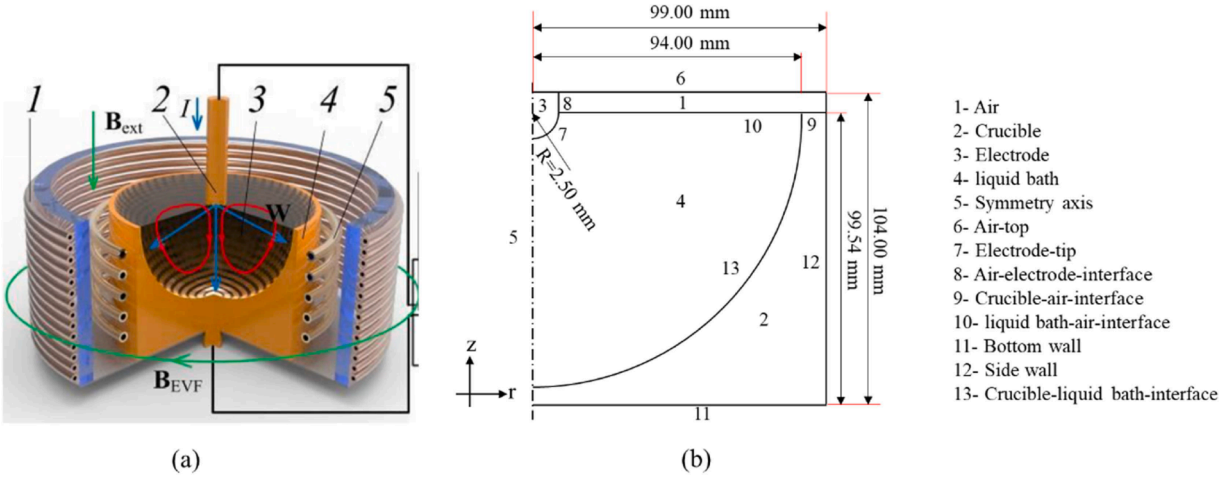


**Fig. 1.** (a) Experimental setup, (b) the 3D axisymmetric domain. 1-solenoid, 2- electrode, 3-eutectic alloy In-Ga-Sn, 4- hemispherical container, 5-heat exchanger [31].

minimal ripple effects. Moreover, the integration of a system comprising Maxwell coils served to counterbalance the Earth's axial magnetic field. This integration facilitated the establishment of a uniform magnetic field along the $z$-axis, achieved through the placement of Helmholtz coils. For further information, please refer to the citation provided [36]. The numerical simulations were conducted under the following assumptions:

i. A 3D axisymmetric swirl model was adopted to represent the flow behavior.
ii. The presence of an arc around the electrode tip was disregarded.
iii. The movement of the liquid-air interface was neglected, treating it as a stationary boundary.
iv. The system was assumed to be isothermal, with no temperature gradients considered.
v. Flow equations were not solved in the air zone, focusing solely on the conductive liquid domain.

In the axisymmetric condition, the magnetic field (B) can be solved by considering only the tangential component of the magnetic field ($B_\theta$) and the magnetic potential vector ($A_\theta$). By utilizing this approach, the behavior of the magnetic field within the system can be effectively determined and analyzed, providing valuable insights into the electromagnetic phenomena under consideration [11,38].

$$\frac{\partial B_\theta}{\partial t}+\frac{\partial(u_z B_\theta)}{\partial z}+\frac{\partial(u_r B_\theta)}{\partial r}=\frac{\partial}{\partial r}\left(\frac{1}{r\sigma\mu_0}\frac{\partial(rB_\theta)}{\partial r}\right)+\frac{\partial}{\partial z}\left(\frac{1}{\sigma\mu_0}\frac{\partial(B_\theta)}{\partial z}\right)-\frac{u_r B_\theta}{r}-\frac{B_\theta}{\sigma\mu_0 r^2}-\frac{\partial(u_\theta B_z)}{\partial z}-\frac{\partial(u_\theta B_r)}{\partial r}, \tag{1}$$

$$\frac{\partial A_\theta}{\partial t}+\frac{\partial(u_z A_\theta)}{\partial z}+\frac{\partial(u_r A_\theta)}{\partial r}=\frac{\partial}{\partial r}\left(\frac{1}{r\sigma\mu_0}\frac{\partial(rA_\theta)}{\partial r}\right)+\frac{\partial}{\partial z}\left(\frac{1}{\sigma\mu_0}\frac{\partial(A_\theta)}{\partial z}\right)-\frac{u_r A_\theta}{r}-\frac{A_\theta}{\sigma\mu_0 r^2}\ . \tag{2}$$

In the given equations, $t$ represents time, $u_r,u_\theta,u_z$ represent the radial, tangential, and axial components of the velocity field, respectively. Similarly, $B_r,B_\theta,B_z$ represent the radial, tangential, and axial components of the magnetic field. The symbols $\mu_0$ and $\sigma$ represent the magnetic permeability and electric conductivity. Finally, $r$, $\theta$, $z$ represent the radial, tangential, and axial coordinates.

The poloidal current density components ($J_r$, $J_z$) and toroidal component of current density ($J_\theta$) could be calculated as follows [11]:

$$J_r=-\frac{1}{\mu_0}\frac{\partial B_\theta}{\partial z}, \tag{3}$$

$$J_\theta=-\sigma\left(\frac{\partial A_\theta}{\partial t}+u_z\frac{\partial A_\theta}{\partial z}+\frac{u_r}{r}\frac{\partial(rA_\theta)}{\partial r}\right), \tag{4}$$

$$J_z=\frac{1}{\mu_0 r}\frac{\partial(rB_\theta)}{\partial r}\ . \tag{5}$$

Eventually, Lorentz forces [39] are explicitly computed and added as source terms to the momentum conservation equations:

$$F_r=J_\theta B_z-J_z B_\theta, \tag{6}$$

$$F_\theta=J_z B_r-J_r B_z, \tag{7}$$

$$F_z=J_r B_\theta-J_\theta B_r. \tag{8}$$

where $F_r,F_\theta,F_z$ are radial, tangential, and axial components of the Lorentz force.

Navier–Stokes equations in 3D axisymmetric swirl cylindrical coordinates are as follows [39]:

$$\frac{1}{r}\frac{\partial(ru_r)}{\partial r}+\frac{\partial(u_z)}{\partial z}=0, \tag{9}$$

$$\frac{\partial(\rho u_r)}{\partial t}+\frac{1}{r}\frac{\partial(r\rho u_z u_r)}{\partial x}+\frac{1}{r}\frac{\partial(r\rho u_r u_r)}{\partial r}=-\frac{\partial P}{\partial r}+\frac{1}{r}\frac{\partial}{\partial z}\left[r\mu\left(\frac{\partial u_z}{\partial r}+\frac{\partial u_r}{\partial z}\right)\right]-\frac{2\mu u_r}{r^2}+\frac{\rho u_\theta^2}{r}+\frac{1}{r}\frac{\partial}{\partial z}\left[r\mu\left(2\frac{\partial u_r}{\partial r}-\frac{2}{3}\left(\frac{1}{r}\frac{\partial(ru_r)}{\partial r}+\frac{\partial u_z}{\partial z}\right)\right)\right]+\frac{2\mu}{3r}\left(\frac{1}{r}\frac{\partial(ru_r)}{\partial r}+\frac{\partial u_z}{\partial z}\right)+F_r, \tag{10}$$

$$\frac{\partial(\rho u_\theta)}{\partial t}+\frac{1}{r}\frac{\partial(r\rho u_z u_\theta)}{\partial z}+\frac{1}{r}\frac{\partial(r\rho u_r u_\theta)}{\partial r}=\frac{1}{r}\frac{\partial}{\partial z}\left[r\mu\frac{\partial u_\theta}{\partial z}\right]+\frac{1}{r^2}\frac{\partial}{\partial r}\left[r^3\mu\frac{\partial}{\partial r}\left(\frac{u_\theta}{r}\right)\right]-\rho\frac{u_r u_\theta}{r}+F_\theta, \tag{11}$$

$$\frac{\partial(\rho u_z)}{\partial t}+\frac{1}{r}\frac{\partial(r\rho u_z u_z)}{\partial z}+\frac{1}{r}\frac{\partial(r\rho u_z u_r)}{\partial r}=-\frac{\partial P}{\partial z}+\frac{1}{r}\frac{\partial}{\partial r}\left[r\mu\left(\frac{\partial u_z}{\partial r}+\frac{\partial u_r}{\partial z}\right)\right]+\frac{1}{r}\frac{\partial}{\partial z}\left[r\mu\left(2\frac{\partial u_z}{\partial z}-\frac{2}{3}\left(\frac{1}{r}\frac{\partial(ru_r)}{\partial r}+\frac{\partial u_z}{\partial z}\right)\right)\right]-\rho g+F_z\ . \tag{12}$$

where $p$ is the static pressure, and μ is viscosity.

The boundary conditions are listed in Table 1, with corresponding boundaries shown in Fig. 1.

The computational domain utilized in the simulations consisted of a total of 83,000 quadrilateral mesh elements. Notably, a finer mesh resolution was employed in the vicinity of the crucible and electrode to accurately capture localized phenomena. The liquid metal used in the study is composed of an Indium-gallium-tin alloy, while the crucible and electrode materials are copper. The specific properties of these materials are provided in Table 2.

### 2.1. Computational procedure

The Finite Volume Method (FVM) was applied to discretize the governing equations within the computational domain. To accommodate specialized boundary conditions and equations, user-defined functions (UDF) were integrated [42]. Discretization methods included Green–Gauss cell-based for gradient calculation, body force weighted for pressure calculation, third-order MUSCL for momentum calculation, and swirl velocity, B-theta, and A-theta. The pressure-velocity coupling was implemented using the PISO scheme. All simulations were conducted transiently with a small time step of $10^{-5}$[s] to ensure

**Table 1**
Boundary conditions.

| Boundary | $B_\theta$ | $A_\theta$ | Flow |
|---|---|---|---|
| Symmetry axis | 0 | 0 | $\frac{\partial u_r}{\partial r}=\frac{\partial u_\theta}{\partial \theta}=\frac{\partial u_z}{\partial z}=0$ |
| Air-top | $B_\theta=\frac{I_0\mu_0}{2\pi r}$ | $\frac{\partial A_\theta}{\partial z}=0$ | - |
| Electrode-tip | - | - | $u_r=u_\theta=u_z=0$ |
| Air-electrode-interface | $B_\theta=\frac{I_0\mu_0}{2\pi r}$ | - | - |
| Crucible-air-interface | - | - | - |
| liquid bath-air-interface | $B_\theta=\frac{I_0\mu_0}{2\pi r}$ | - | $\frac{\partial u_r}{\partial r}=u_\theta=u_z=0$ |
| Bottom wall | $\frac{\partial B_\theta}{\partial z}=0$ | $\frac{\partial A_\theta}{\partial z}=0$ | - |
| Side wall | $B_\theta=\frac{I_0\mu_0}{2\pi r}$ | $A_\theta=\frac{B_z r}{2}$ | - |
| Crucible-liquid bath-interface | - | - | $u_r=u_\theta=u_z=0$ |

**Table 2**
Process parameters and averaged material properties used in the simulations [40,41].

| | |
|---|---|
| In-Ga-Sn (Liquid) | |
| Density | 6482 kg $m^{-3}$ |
| Kinematic viscosity | $4.5 \times 10^{-7}$ $m^2$ $s^{-1}$ |
| Electric conductivity | $3.3 \times 10^6$ Sm |
| Copper (Electrode and crucible) | |
| Electric Conductivity | $4.5 \times 10^7$ Sm |
| Process parameters | |
| Electric current ($I_0$) | 50–400 A |
| External magnetic field ($B_z$) | 0.001–10 mT |
| magnetic permability ($\mu_0$) | $4\pi \times 10^{-7}$J $m^{-1}$ $A^{-2}$ |

convergence.

To verify the simulation results, a comparison was made with the experimental data obtained by Vinogradov et al. [43]. In their laboratory, they developed fiber-optical transducers to measure the axial velocity at a depth of 10 mm on the axis near the electrode. Specifically, the measurements were conducted for a current of 400 A and a magnetic field strength of 0.5 mT. The experimental data served as a benchmark for validating the accuracy and reliability of the simulation results. More detailed information regarding the validation process will be provided in Section 3.1.Validation.

By analyzing the behavior of conductive flow within a hemisphere under different external magnetic fields and electric currents, our study offers valuable insights for optimizing industrial processes such as Electroslag Remelting (ESR) [5–8] and Vacuum Arc Remelting (VAR) [9–12]. Understanding the flow dynamics can lead to improved efficiency, reduced energy consumption, and enhanced product quality in these manufacturing processes. Additionally, it's worth noting that the temperature of the liquid within the pool, which corresponds to the hemispherical container, is considerably high in VAR and ESR. This poses challenges for measuring temperature and velocity accurately, unlike in Ga-In-Sn, which is liquid at room temperature.

## 3. Results and discussions

The Lorentz forces in the system can be classified into two types: poloidal and toroidal. The poloidal Lorentz force ($\vec{F}_{pol}$) consists of components in the radial ($F_r$) and axial ($F_z$) directions, as illustrated by the vector field on the left side of Fig. 2(a). On the other hand, the toroidal Lorentz force ($\vec{F}_{tor}$) only exists in the tangential direction ($F_\theta$), as illustrated by the vector field on the right side of Fig. 2(a). The flow structure is influenced by the relative strength of these two forces. It is well known when the poloidal force dominates over the toroidal Lorentz force, it drives the flow from the liquid's free surface toward the electrode, generating a strong jet that flows toward the bottom. Conversely, when the toroidal Lorentz force becomes stronger, it induces a centrifugal acceleration $\frac{u_\theta^2}{r} = \frac{swirl\ velocity^2}{radial\ position}$, perpendicular to the azimuthal direction. This leads to the formation of a secondary flow called vortex backdown flow (VBF) [38]. The interplay between these two forces determines the characteristics and behavior of the flow within the system.

Considering Ampère's law (Eqs. (3)–(5)), the electric current density can be derived from the magnetic field distribution. In the present study, the electric current lines enter the computational domain from the electrode and follow a path toward the crucible, eventually exiting from the bottom of the crucible (as shown in Fig. 2(b)). The electric current density exhibits a peak value near the axis and gradually decreases radially away from the axis towards the crucible side wall. Herein, all investigated cases exhibit an identical distribution of electric current density.

To enhance the comprehension of the flow structure in the hemispherical container and its dependence on the electric current and magnetic field, several concepts proposed by Kharicha et al. [38] are introduced. These concepts provide valuable insights into the underlying mechanisms governing the flow behavior in such systems. These concepts are as follows:

1- Rope tornado: The rope tornado refers to a flow structure characterized by the presence of a toroidal velocity component concentrated around the axis of symmetry. This flow structure exhibits similarities to the Electro-Vortex Flow (EVF) but with the additional feature of a distinct toroidal velocity component.
2- Tornado: The tornado flow structure is characterized by the presence of a Vortex Breakdown Flow (VBF) that rotates in the opposite direction to the EVF. The VBF penetrates and displaces the EVF away from the center line. The tornado is identified by a region of high swirl along the centerline, indicating the presence of intense vortex activity.
3- Cyclone: The cyclone flow structure is characterized by the interaction between the VBF and the tornado. The VBF acts in opposition to the tornado, particularly near the crucible where the tornado weakens. In this region, the VBF has the capability to disrupt the tornado structure. As the magnetic field increases, the VBF becomes stronger, causing the concentration of swirl velocity to shift away from the center of the container.
4- Inverted tornado: By further increasing the magnetic field beyond the cyclone case, a new Vortex Breakdown Flow (VBF) emerges near the bottom of the electrode. This newly formed VBF accumulates sufficient angular momentum, leading to the development of an inverted tornado within the existing cyclone structure. The inverted

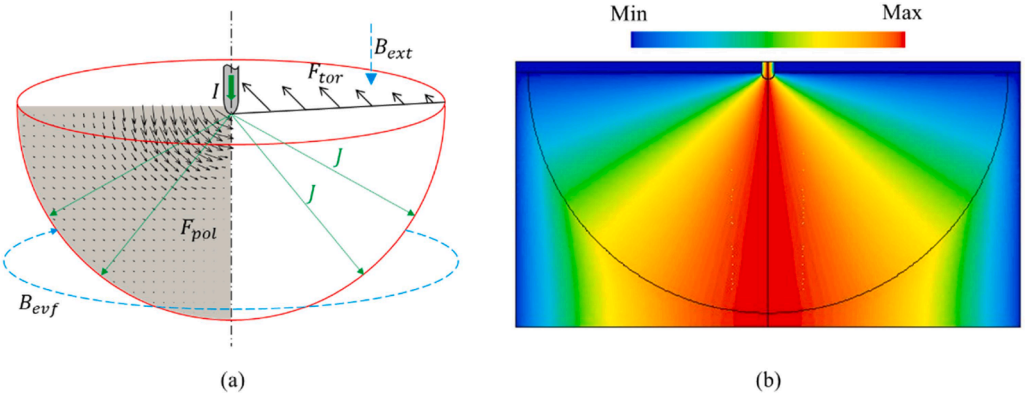


**Fig. 2.** (a) Componnet of Lorentz forces including poloidal and toroidal in the hemispherical container. (b) The electric current flows from the electrode to the crucible.

tornado exhibits a reversed rotational direction compared to the cyclone and is characterized by a distinct concentration of swirl velocity.

Figs. 3 and 4 provide a visual representation of the flow structure captured by our model, illustrating the poloidal and toroidal velocities. These figures offer insights into the flow dynamics. Figs. 3(a), (b), 4(a), and (b) describe the flow structures of the Rope tornado, Tornado, Cyclone, and Inverted tornado, respectively. Herein, the magnetic field is varied while keeping the electric current intensity constant. Each case represents a different magnetic field strength, enabling us to study the specific influence of the magnetic field on the flow behavior

Fig. 3(a) illustrates the flow structure characterized as a rope tornado. This configuration is distinguished by the constriction of both poloidal and toroidal flows around the axis, resulting in a pronounced jet flow from the electrode toward the crucible. The absence or limited presence of opposing forces allows the flow structure to remain stable. The poloidal contour plot reveals the extensive coverage of the Electro-Vortex Flow (EVF) throughout the domain, exhibiting a clockwise rotation pattern. In Fig. 3(b), the emergence of a secondary vortex is observed as the magnetic field strength increases. This vortex, known as the vortex breakdown flow (VBF), appears on the side of the axis. The VBF exhibits a distinct behavior by exerting pressure on the primary EVF. The VBF displaces the EVF away from the center to occupy the region closer to the axis. This interaction between the VBF and EVF demonstrates the dynamic changes occurring within the flow structure.

As shown in Fig. 4(a), the augmentation of the magnetic field intensity instantaneously alters the Lorentz forces acting along the radial ($r$) and azimuthal ($\theta$) directions. In this scenario, the fluid experiences accelerated rotation around the axis due to the amplification of the toroidal force. Consequently, the centrifugal force intensifies, causing the fluid to migrate away from the central region. Simultaneously, the diminishing radial forces with increasing magnetic field strength become insufficient to maintain the fluid in a tightly concentrated vortex shape along the axis. As a consequence, the emergence of a substantial cyclonic vortex, characterized by pronounced rotation in the $\theta$ direction, becomes predicted. Concurrently, within the poloidal plane, the EVF experiences a reduction in strength, while the VBF progressively dominates a larger portion of the domain.

Based on the swirl velocity contour illustrated in Fig. 4(b), it is evident that with a continued increase in the magnetic field, a novel vortex emerges within the core of the cyclone. This phenomenon can be attributed to the observation that the flow within the central region of the cyclone experiences a relatively tranquil state in close proximity to the electrode. As one moves along the axis from the electrode towards the crucible, this calm region progressively narrows. Consequently, the EVF once again becomes prominent and gives rise to a vortex structure resembling an inverted cone, often referred to as an inverted tornado. Moreover, by examining the poloidal velocity contour, it becomes apparent that the VBF, which serves as the dominant vortex within the domain, exhibits a counterclockwise rotation. Adjacent to this primary vortex and in close proximity to the axis, a localized and concentrated EVF can be observed rotating in the opposite direction.

Previously, four different flow structures were described by maintaining a constant electric current and varying the magnetic field. The impact of the electric current on the flow structure was also investigated while keeping the magnetic field constant, as shown in Fig. 5. For this comparative analysis, four cases were considered, employing a low magnetic field to mitigate the influence of the induced electric field present in the $A_\theta$ equation (Eq. (2)). By referring to the definition of Lorentz forces (Eqs. (6)–(8)), it is evident that the magnitude of these forces can be directly altered by increasing the electric current.

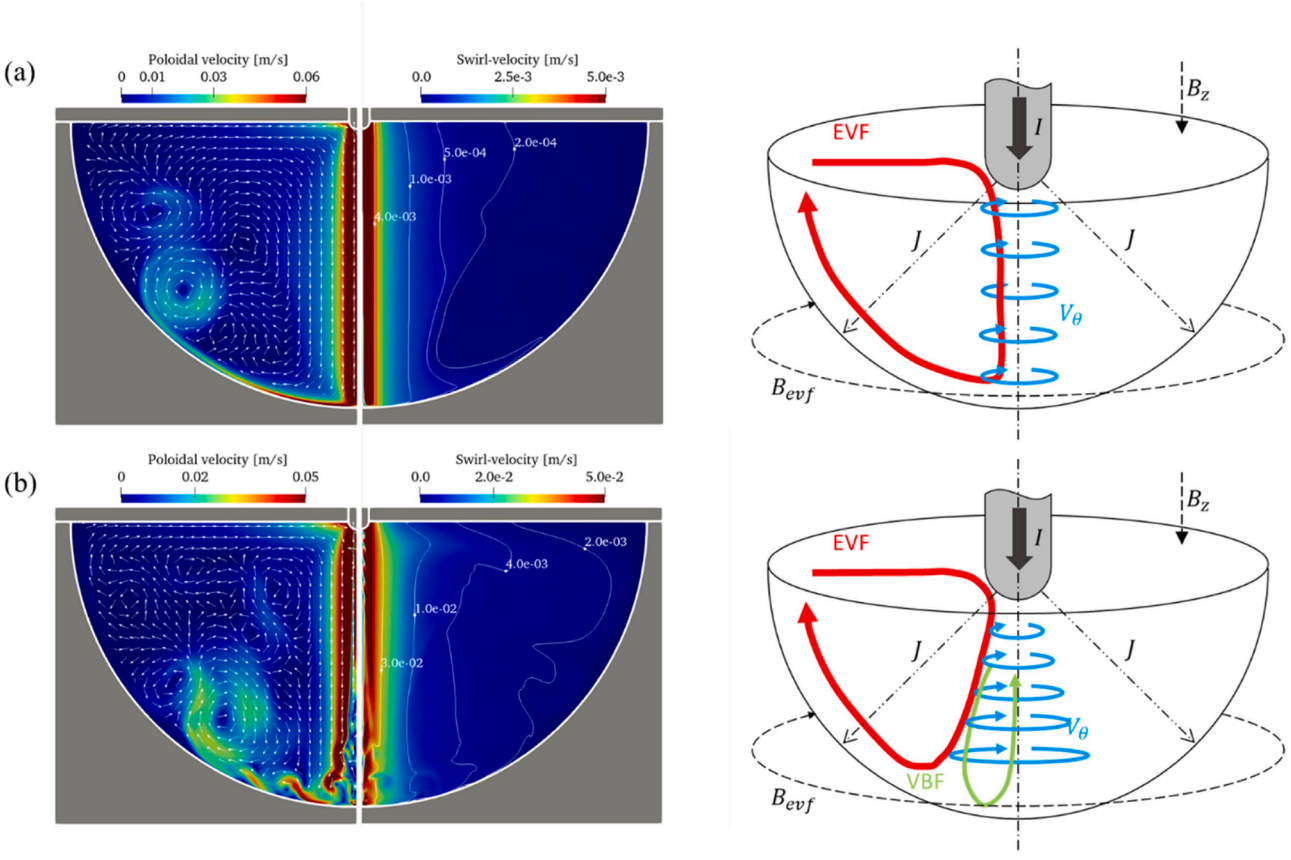


**Fig. 3.** (Left) contour of poloidal velocity and contour of swirl velocity. (Right) Schematic of the flow field structure. (a) Represent the rope tornado at $I = 200A$, $B_z = 1 \times 10^{-5}T$, and (b) represent the tornado at $I = 200A$, $B_z = 1 \times 10^{-4}T$.

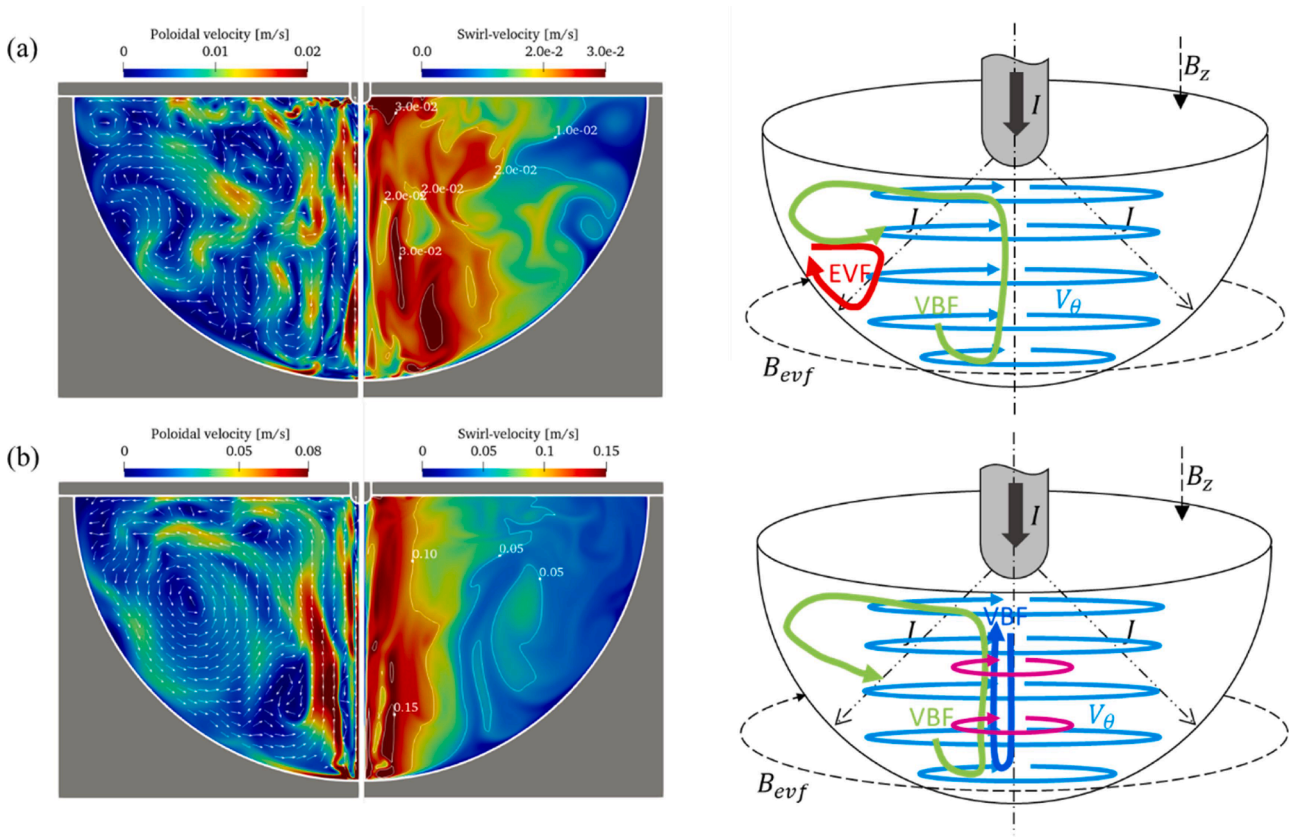


**Fig. 4.** (Left) contour of poloidal velocity and contour of swirl velocity. (Right) Schematic of the flow field structure. (a) Represent the cyclone at $I = 200A$, $B_z = 1 \times 10^{-3}T$, and (b) represent the inverted tornado at $I = 200A$, $B_z = 1 \times 10^{-2}T$.

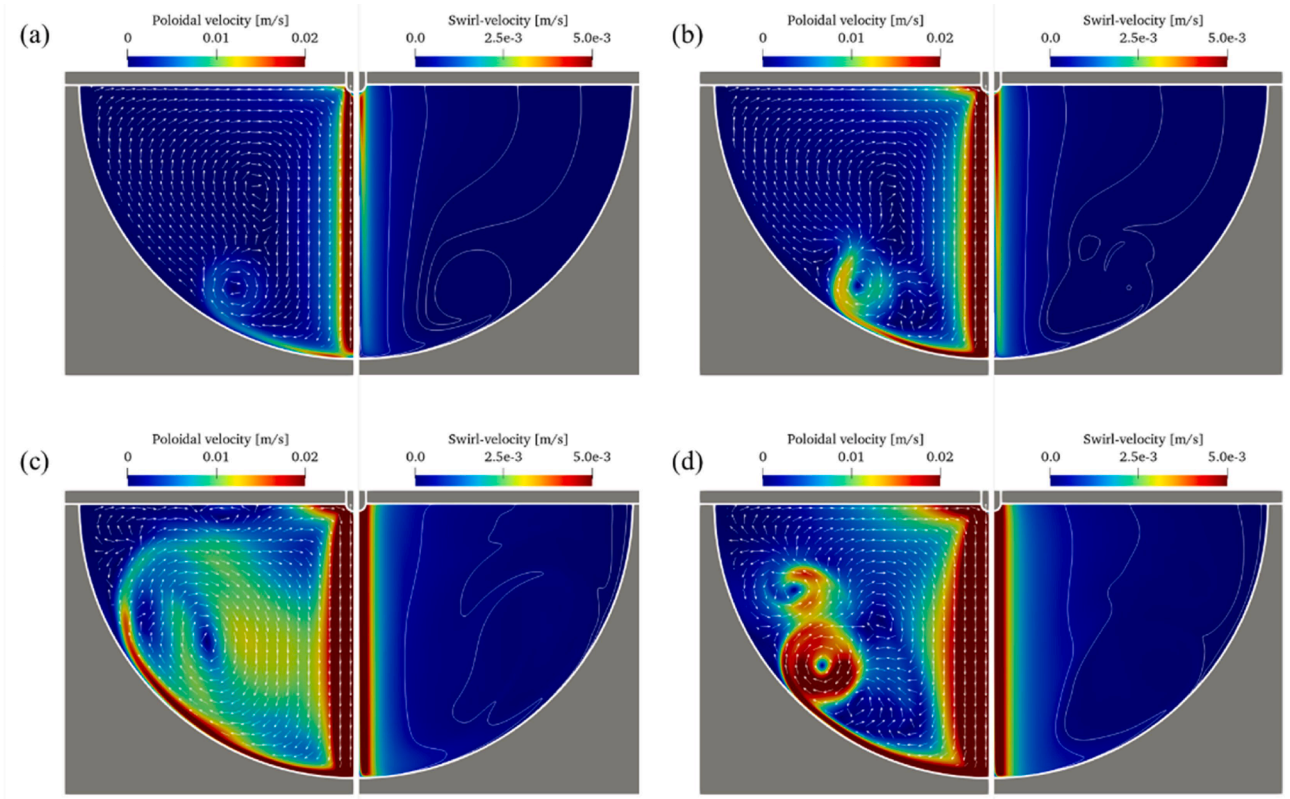


**Fig. 5.** Left is the contour of poloidal velocity, and right is the contour of swirl velocity. Considering constant magnetic field $1 \times 10^{-5}$ mT. The electric current intensity is shown for (a) 50 A, (b) 100 A, (c) 150 A, and (d) 200 A respectively.

However, due to the assumption of a low magnetic field, the flow structure is constrained to that of a rope tornado. The comparative analysis of the four swirl velocity contours, illustrated in Fig. 5, demonstrates a clear correlation between the strength of the tornado and the increase in electric current. It is evident that as the electric current is increased, the intensity of the tornado is amplified accordingly.

At lower electric currents, the tornado primarily occupies a region in close proximity to the electrode. However, as the electric current is elevated, the tornado gains power and expands its occupied area, extending from the electrode toward the crucible. This phenomenon illustrates how the increased electric current influences the spatial distribution and extent of the tornado within the system. Furthermore, from the analysis of the poloidal velocity contour, it can be inferred that as the electric current increases, the EVF in the respective region becomes stronger and exerts influence over the entire area. This heightened EVF leads to an accelerated clockwise rotation of the fluid at a greater velocity. The observed relationship between electric current and the strength of EVF highlights the significant role of the current intensity in shaping the flow dynamics.

Several simulations were performed to further explore the dynamics of the system. A parametric study was conducted to assess the system behavior across a wider range of magnetic fields and electric currents. The parameters used in our simulations are presented as black points in Fig. 6, providing a graphical representation of the results obtained from the study. These points serve as indicators of the simulated data, allowing for a clear visualization of the observed outcomes. This chart effectively illustrates the transformation of the flow structure as the magnetic field strength increases for different electric currents. It demonstrates the progression from a rope tornado to a tornado, followed by a cyclone, and ultimately culminating in an inverted tornado.

Additionally, it was observed that the transition in the flow structure does not occur at the same magnetic field strength for different electric currents. For instance, the shift from a rope tornado to a tornado is observed at approximately 0.01 mT for an electric current of 50 A, while the same transition occurs at around 0.05 mT for an electric current of 200 A, as shown in Fig. 6. This finding indicates that the critical magnetic field strength required for the transition varies depending on the magnitude of the electric current.

The qualitative assessment of the flow structure formed the foundation for the classification presented in Fig. 6. However, to quantify the flow structure, it is necessary to consider the amount of kinetic energy in the poloidal ($K_p$) and toroidal ($K_t$) directions as follows:

$$K_p = \int \frac{\rho(u_r{}^2 + u_z{}^2)}{2}\, dv \tag{13}$$

$$K_t = \int \frac{\rho(u_\theta{}^2)}{2}\, dv \tag{14}$$

Fig. 7 shows the computed results of the kinetic energy of the fluid against the magnetic field. Fig. 7(a) illustrates the relationship between the magnetic field and the poloidal kinetic energy. It indicates that as the magnetic field increases within the range of 0.01 mT to 0.1 mT, there is a slight rise in the quantity of poloidal kinetic energy. On the other hand, Fig. 7(b) shows the toroidal kinetic energy and its variation. It demonstrates that the toroidal kinetic energy experiences significant changes during the range of 0.01 mT to 0.1 mT, which corresponds to the transition from a rope tornado to a tornado.

In the magnetic field range of 0.1 mT to 1 mT, Fig. 7(a) demonstrates a significant decrease in the poloidal kinetic energy. Meanwhile, Fig. 7 (b) reveals that the toroidal kinetic energy remains relatively constant during this range. This observation indicates the presence of a cyclone within the domain. The observed decrease in poloidal kinetic energy can be attributed to the competition between the two vortices present in the system. As the cyclone structure emerges and becomes dominant, it potentially opposes the existing flow patterns, leading to a decrease in the poloidal kinetic energy. This competition between the vortices results in redistribution and alteration of the flow dynamics, influencing the overall energy distribution within the system.

Afterward, as the magnetic field is further increased from 1 mT to 10 mT, a transition in the flow structure occurs from a cyclone to an inverted tornado. During this stage, it is notable that both toroidal and poloidal kinetic energy experience a significant increase.

Based on observations, fluid structures occasionally exhibit fluctuations between two distinct structures. This behavior can be attributed to internal oscillation and inertia within the system. This phenomenon was also highlighted by Klementyeva et al. [31]. In their experimental setup, noting the occurrence of these fluctuations at the measured point located 10 mm below the electrode within the fluid. To visually represent the overlapping of the two structures, Fig. 7 incorporates a symbolic representation using different colors and a dashed line. Each stage is shown with a distinct color, and the dashed line illustrates the overlap between the structures. This graphical representation aids in conveying the transitional nature of the flow and the coexistence of different flow patterns during the observed stages.

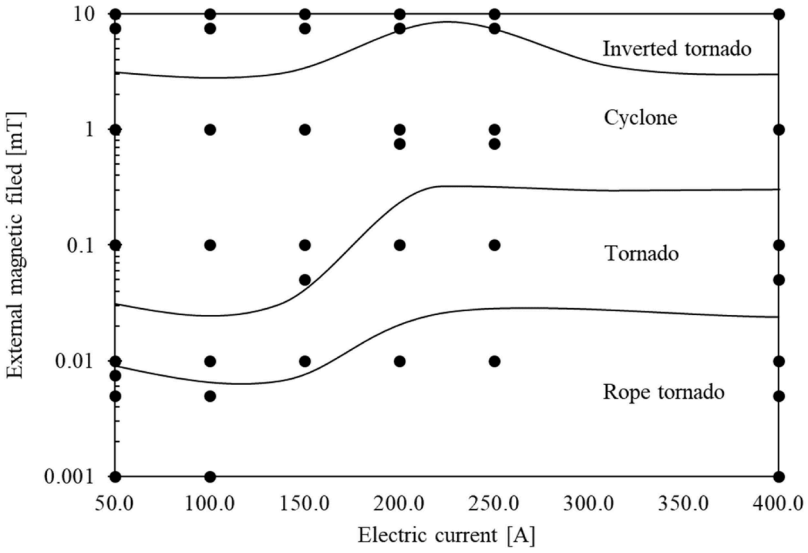


**Fig. 6.** Classification of results into rope tornado, tornado, cyclone, and inverted tornado.

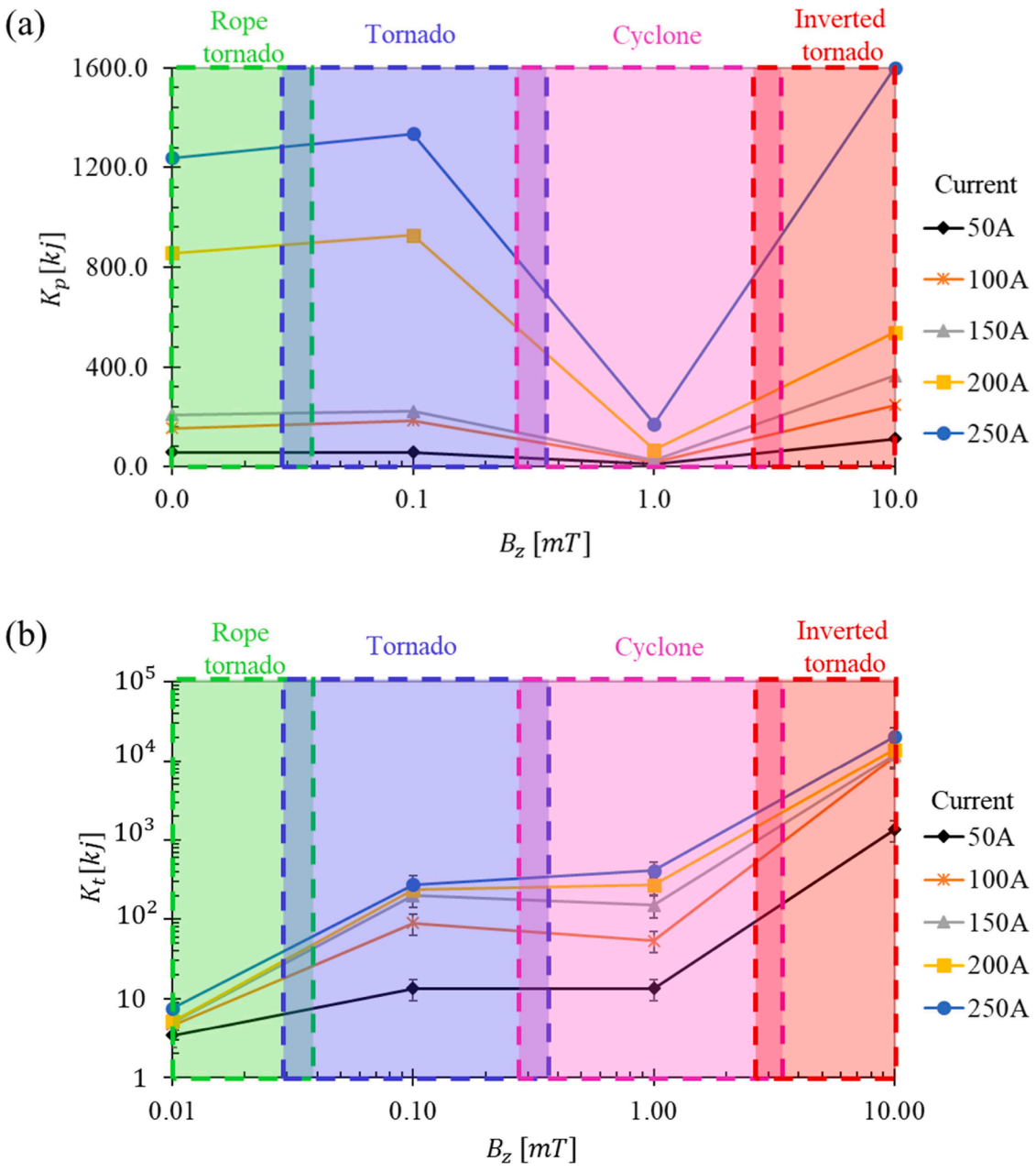


**Fig. 7.** (a) Poloidal Kinetic energy versus magnetic field. (b) Toroidal Kinetic energy versus magnetic field.

### 3.1. Validation

The simulations were conducted under the same conditions as Vinogradov et al. [43] experimental setup, with a current of 400 A and a magnetic field strength of 0.5 mT. Based on the results illustrated in Fig. 6, the flow structure for this particular case corresponds to the cyclone region. To further evaluate and compare our simulation with experimental data, Measurements of the axial velocity were conducted at the specified location.

To account for potential manufacturing and testing errors in laboratory setups, The measurements were expanded to two additional locations. These locations were situated 1 mm and 5 mm radially away from the axis. By collecting velocity data at these positions, the aim was to obtain a more comprehensive understanding of the flow dynamics and minimize any potential sources of uncertainty in the experimental measurements. The location of these three points is shown in Figs. 8(a) and 9(a). Figs. 8(b), (c) and (d) demonstrate the fluctuating of the fluid flow.

To validate the simulation results against experimental data, the following observations are utilized:

- Firstly, during the initial five seconds, the axial velocity exhibits a positive value, indicating the presence of a clockwise Electro-Vortex Flow (EVF) within the domain. This observation is supported by supplementary videos and Fig. 8, depicting consistent findings across all three measurement points (8b, 8c, and 8d).
- Secondly, fluctuation is evident not only in the experimental data but also in our simulations. Moreover, it is observed that the level of fluctuation is greater at the first point compared to the second point, and similarly, the second point exhibits more fluctuation than the third point. Generally, as the distance from the axis line increases, the degree of fluctuation tends to decrease.
- Thirdly, after approximately five seconds, the influence of the VBF intensifies and leads to a reversal in the flow direction, causing the

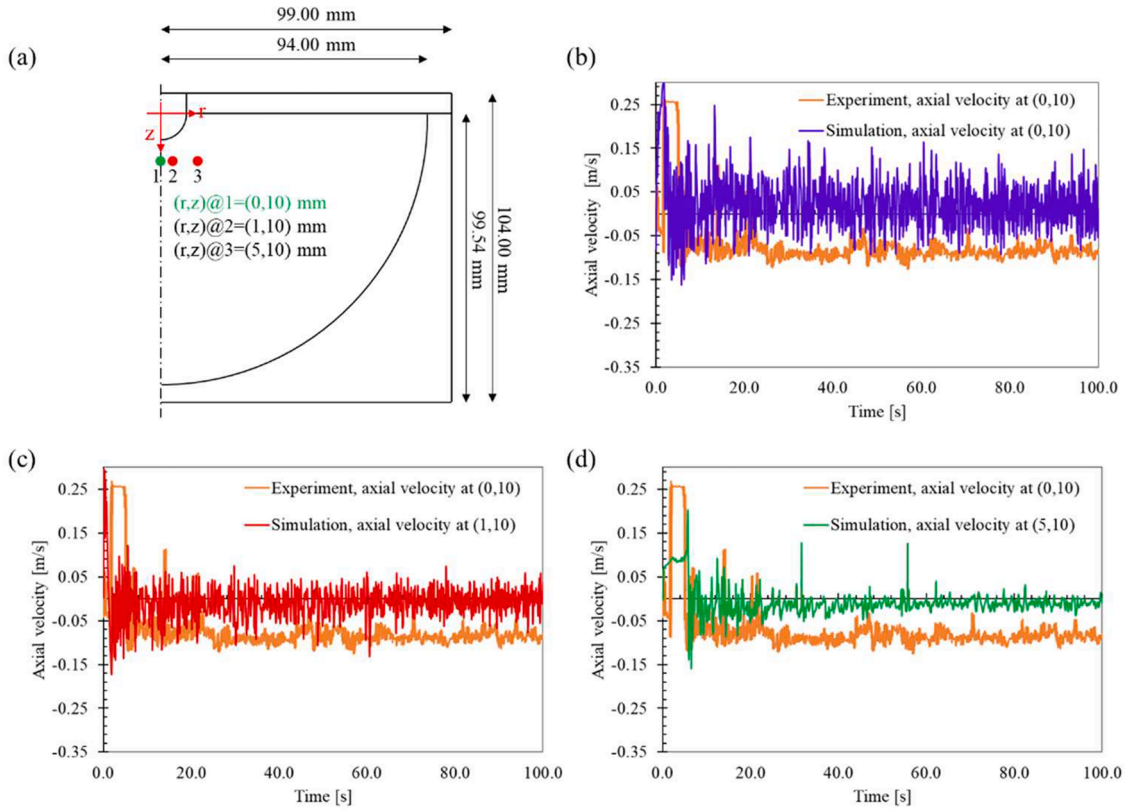


**Fig. 8.** Comparison of axial velocities between experimental measurements and simulation results.(a) The spatial position of the measured point: the green point represents the experimental measurement location, while the red points correspond to two additional measurement points from the simulation. (b), (c), and (d) illustrate the temporal variation of axial velocity as a function of time for all three points, including the experimental measurement.

fluid to rotate in a counterclockwise manner. Subsequently, the flow rate exhibits fluctuations around a relatively stable value. In the experimental data, this value is approximately 0.1 m $s^{-1}$. However, in the simulation results from the three different measurement points, the flow rate ranges from 0 to ca. 0.01 m $s^{-1}$.

It's crucial to acknowledge the disparity between the experimental and simulated values, suggesting potential differences in the accuracy and precision of the two approaches. This variation may be attributed to the following factors:

- The simulation was conducted in a 3D axisymmetric swirl setting, the laboratory setup represents a full three-dimensional environment. This simplification in the simulation could potentially contribute to the differences observed between the laboratory results and the simulated samples. This discrepancy highlights the inherent limitations of the simulation approach and emphasizes the need for further refinement and consideration of full three-dimensional effects in future simulations to better align with experimental observations.
- Furthermore, in the simplification, the dynamic motion of the fluid interface was disregarded. It is important to note that the fluid interface is not static but exhibits movement, as indicated by Kharicha et al. [35]. This disparity in the interface's behavior could potentially lead to discrepancies between simulation and experimental results.
- On the other hand, it is plausible that the sensor utilized by the aforementioned group may not have exclusively measured the axial velocity component. It is possible that the recorded velocity value represents the magnitude of all velocity components rather than solely the axial velocity. Such a scenario could lead to discrepancies when comparing these experimental measurements with the simulation results, which specifically focus on the axial velocity component.

To address the potential discrepancy between the experimental velocity measurement and the simulation results, a comparison was conducted between the experimental velocity and the velocity magnitude obtained from the simulation at three different points. As shown in Fig. 9, at point 1, precisely located on the axis, the axial component of velocity dominates, while other velocity components remain relatively small. This dominance makes distinguishing between axial velocity Fig. 8(b) and velocity magnitude Fig. 9(b) challenging, although there is approximately a five percent difference between the two. Within the initial five seconds, a counterclockwise rotation is observed, consistent with experimental measurements. As once move 1 mm away from the axis, the flow direction remains similar to that at the axis point, with fluctuations diminishing. However, at point 3, situated further from the axis, not only does the flow direction align with experimental data, but the velocity magnitude also closely matches experimental values. As move away from the axis and approach point three, the similarity between the experimental and simulated results increases. Notably, in Fig. 9(d), it is evident that the simulation results exhibit a good agreement with the experimental data.

## 4. Conclusion

This study conducts numerical simulations aimed at analyzing the behavior of conductive flow within a hemisphere under different external magnetic fields and electric currents. The key findings of the publication are outlined below:

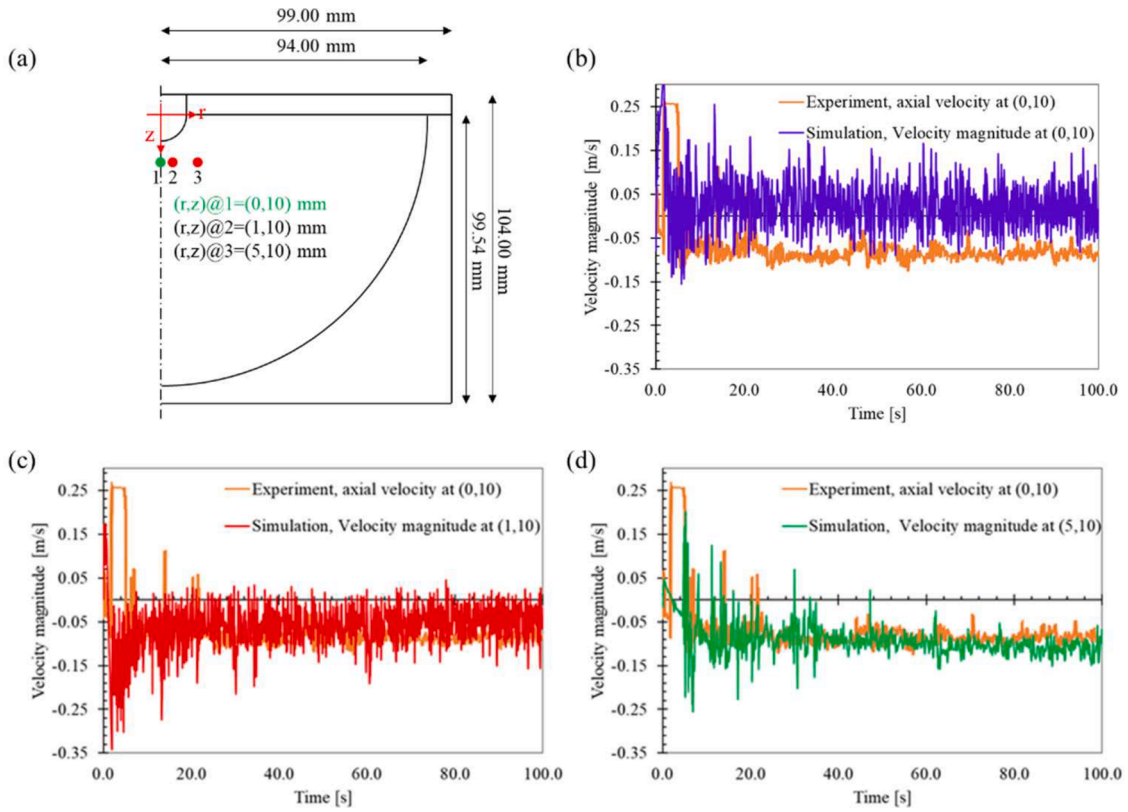


**Fig. 9.** Comparison of velocity magnitude between experimental measurements and simulation results. (a) The spatial position of the measured Point: the green point represents the experimental measurement location, while the red points correspond to two additional measurement points from the simulation. (b), (c), and (d) illustrate the temporal variation of velocity magnitude as a function of time for all three points, including the experimental measurement.

- The simulations revealed the presence of four distinct flow types: the rope tornado, tornado, cyclone, and inverted tornado, each observed with increasing magnetic field strength.
- The results contribute to the categorization of flow structures considering different magnetic fields and electric current intensities.
- The kinetic energy analysis was employed to assess and categorize the toroidal and poloidal kinetic energy components within the domain. It was observed that: As the magnetic field increased within the range of 0.01 mT to 0.1 mT, there was a slight rise in the quantity of poloidal kinetic energy, while the toroidal kinetic energy underwent significant changes. In the magnetic field range of 0.1 mT to 1 mT, a noteworthy decrease in poloidal kinetic energy was observed, whereas the toroidal kinetic energy remained relatively constant. Subsequently, with a further increase in the magnetic field from 1 mT to 10 mT, both toroidal and poloidal kinetic energy experienced a significant increase.
- The simulation results were compared with experimental data for a specific case involving 400 A and 0.5 mT. Velocity analyses were conducted at three locations, revealing that the similarity between the experimental and simulated results increased as one moved away from the axis.

The simulations results can assist engineers in improving processes such as Electroslag Remelting (ESR) and Vacuum Arc Remelting (VAR), which involve a hemispherical pool. While the comparison between experimental and simulation results indicated a relatively satisfactory agreement, it's crucial to acknowledge a fundamental disparity: our simulations were based on a 3D axisymmetric swirl model, whereas the laboratory setup inherently operated in three dimensions. This discrepancy highlights a primary limitation of our study. To overcome this limitation and enhance the fidelity of our simulations, future research endeavors could involve conducting full 3D simulations.

## Funding

The authors acknowledge financial support from the Austrian Federal Ministry of Economy, Family and Youth and the National Foundation for Research, Technology and Development within the framework of the Christian-Doppler Laboratory for Metallurgical Applications of Magneto hydrodynamics.

## CRediT authorship contribution statement

**M. Abdi:** Conceptualization, Methodology, Investigation, Software, Visualization, Writing – original draft, Validation. **E. Karimi-Sibaki:** Writing – review & editing. **C. Sommitsch:** Supervision. **H. Barati:** Methodology, Software. **M. Al-Nasser:** Methodology, Software. **M. Wu:** Supervision. **I. Teplyakov:** Validation, Data curation. **A. Kharicha:** Conceptualization, Methodology, Supervision, Writing – review & editing, Validation, Data curation, Project administration.

## Declaration of competing interest

The authors declare that they have no known competing financial interests or personal relationships that could have appeared to influence the work reported in this paper.

## Data availability

No data was used for the research described in the article.

## Supplementary materials

Supplementary material associated with this article can be found, in the online version, at doi:10.1016/j.ijft.2024.100721.

## References


[1] L. Minkin, D. Sikes, Measuring the magnetic field vector of earth, Phys. Teach. 60 (3) (2022) 200–201.
[2] R. Islas, T. Heine, G. Merino, The induced magnetic field, Acc. Chem. Res. 45 (2) (2012) 215–228.
[3] A.A. Tzavaras, H.D. Brody, Electromagnetic stirring and continuous casting—achievements, problems, and goals, JOM 36 (3) (1984) 31–37.
[4] V. Bojarevičs, J.A. Freibergs, E.I. Shilova, E.V. Shcherbinin, Electrically Induced Vortical Flows, 9, Springer Netherlands, Dordrecht, 1989.
[5] J. Chaulet, A. Kharicha, S. Charmond, B. Dussoubs, S. Hans, M. Wu, et al., A 2D multiphase model of drop behavior during electroslag remelting, Metals (Basel) 10 (4) (2020).
[6] E. Karimi-Sibaki, A. Kharicha, A. Vakhrushev, M. Wu, A. Ludwig, J. Bohacek, Investigation of effect of electrode polarity on electrochemistry and magnetohydrodynamics using tertiary current distribution in electroslag remelting process, J. Iron Steel Res. Int. 28 (12) (2021) 1551–1561.
[7] E. Karimi-Sibaki, A. Kharicha, M. Wu, A. Ludwig, J. Bohacek, A numerical investigation on the electrochemical behavior of CaO and $Al_2O_3$ in the ESR slags, Metall. Mater. Trans. B 51 (3) (2020) 871–879.
[8] C. Schubert, M. Eickhoff, H. Pfeifer, Numerical simulations of the molten metal droplet formation in the electroslag remelting process with a rotating electrode, Steel Res. Int. 93 (12) (2022).
[9] E. Karimi-Sibaki, A. Kharicha, M. Wu, A. Ludwig, J. Bohacek, A parametric study of the vacuum arc remelting (VAR) process: effects of arc radius, side-arcing, and gas cooling, Metall. Mater. Trans. B 51 (1) (2020) 222–235.
[10] E. Karimi-Sibaki, A. Kharicha, A. Vakhrushev, M. Abdi, M. Wu, A. Ludwig, et al., Numerical modeling and experimental validation of the effect of arc distribution on the as-solidified Ti64 ingot in vacuum arc remelting (VAR) process, J. Mater. Res. Technol. 19 (2022 Jul 1) 183–193.
[11] E. Karimi-Sibaki, A. Kharicha, M. Abdi, A. Vakhrushev, M. Wu, A. Ludwig, et al., A numerical study on the influence of an axial magnetic field (AMF) on vacuum arc remelting (VAR) process, Metall. Mater. Trans. B 52 (5) (2021) 3354–3362.
[12] P.O. Delzant, P. Chapelle, A. Jardy, J. Jourdan, J. Jourdan, Y Millet, Investigation of arc dynamics during vacuum arc remelting of a Ti64 alloy using a photodiode based instrumentation, J. Mater. Process. Technol. 266 (2019) 10–18.
[13] W. Herreman, C. Nore, P. Ziebell Ramos, L. Cappanera, J.L. Guermond, N Weber, Numerical simulation of electrovortex flows in cylindrical fluid layers and liquid metal batteries, Phys. Rev. Fluids 4 (11) (2019) 113702.
[14] N. Weber, M. Nimtz, P. Personnettaz, A. Salas, T. Weier, Electromagnetically driven convection suitable for mass transfer enhancement in liquid metal batteries, Appl. Therm. Eng. 143 (2018) 293–301.
[15] T. Weier, A. Bund, W. El-Mofid, G.M. Horstmann, C.C. Lalau, S. Landgraf, et al., Liquid metal batteries—Materials selection and fluid dynamics, in: IOP Conference Series: Materials Science and Engineering, Institute of Physics Publishing, 2017.
[16] N. Weber, C. Duczek, G.M. Horstmann, S. Landgraf, M. Nimtz, P. Personnettaz, et al., Cell voltage model for Li-Bi liquid metal batteries, Appl. Energy 309 (2022) 118331.
[17] A.D. Sneyd, Interfacial instabilities in aluminium reduction cells, J. Fluid Mech. 236 (111) (1992 Apr) 111–126. Available from, https://www.cambridge.org/core/product/identifier/S0022112092001368/type/journal_article.
[18] P.A. Davidson, R.I. Lindsay, Stability of interfacial waves in aluminium reduction cells. Essential Readings in Light Metals, Springer International Publishing, 2016, pp. 359–366. Available from, http://link.springer.com/10.1007/978-3-319-48156-2_51.
[19] A. Kharicha, M. Wu, A. Ludwig, MHD instabilities of bath/liquid metal interface, in: Int Conf on Multiphase Flow (ICMF), 2013, 8th.
[20] V. Ranawade, R. Verma, N. Tiwari, K.S. Nalwa, A comprehensive multiphysics approach to model solutal buoyancy, thermal convection, and electro-vortex flow phenomena for liquid metal batteries, J. Energy Storage 85 (2024) 111100.
[21] P. Personnettaz, S. Landgraf, M. Nimtz, N. Weber, T. Weier, Effects of current distribution on mass transport in the positive electrode of a liquid metal battery, Magnetohydrodynamics 56 (2–3) (2020) 247–254.
[22] P. Personnettaz, T.S. Klopper, N. Weber, T. Weier, Layer coupling between solutal and thermal convection in liquid metal batteries, Int. J. Heat Mass Transf. 188 (2022) 122555.
[23] K.Y. Malyshev, E.A. Mikhailov, I.O. Teplyakov, Rapidly convergent series for solving the electrovortex flow problem in a hemispherical vessel, Comput. Math. Math. Phys. 62 (7) (2022) 1158–1170.
[24] Z. Zhang, M. Wu, H. Zhang, A. Ludwig, A. Kharicha, Effect of forced convection on the formation of the as-cast structure and macrosegregation of Sn-10 wt.% Pb alloy: a numerical study, Int. J. Heat Mass Transf. 208 (2023) 124050.
[25] Z. Zhang, M. Wu, H. Zhang, S. Hahn, F. Wimmer, A. Ludwig, et al., Solidification principle in large vertical steel casting under the EMS effect, Metall. Mater. Trans. B 54 (4) (2023) 1870–1885.
[26] H. Zhang, X. Liu, D. Ma, M. Song, A. Ludwig, A. Kharicha, et al., Digital twin for directional solidification of a single-crystal turbine blade, Acta Mater. 244 (2023) 118579.
[27] P.A. Davidson, An Introduction to Magnetohydrodynamics, Cambridge University Press, 2001 [cited 2023 Apr 17]. Available from: https://www.cambridge.org/core/product/identifier/9780511626333/type/book.
[28] D.A. Vinogradov, I.O. Teplyakov, Y.P. Ivochkin, Numerical simulation of the electrovortex flow in the non-inductive approximation under the influence of an external magnetic field, in: Journal of Physics: Conference Series, Institute of Physics Publishing, 2019.
[29] D. Vinogradov, I. Teplyakov, Y. Ivochkin, Calculation of the magnetic field of a current-carrying system, Mathematics 11 (17) (2023) 3623.
[30] P. Frick, S. Mandrykin, V. Eltishchev, I. Kolesnichenko, Electro-vortex flows in a cylindrical cell under axial magnetic field, J. Fluid Mech. 949 (2022) A20.
[31] D.A. Vinogradov, I.O. Teplyakov, Y.P. Ivochkin, A. Kharicha, On the applicability of the electrodynamic approximation in the simulation of the electrovortex flow in the presence of an external magnetic field, J. Phys. Conf. Ser. 1128 (1) (2018) 012112.
[32] V.G. Zhilin, Y.P. Ivochkin, I.O Teplyakov, The problem of swirling of axisymmetric electrovortex flows, High Temp. 49 (6) (2011) 927–929.
[33] A. Shercliff, Fluid motions due to an electric current source, J. Fluid Mech. 40 (1970) 241–250.
[34] K.Y. Malyshev, E.A. Mihailov, I.O Teplyakov, Analytical study of the velocity and pressure of the electrovortex flow in hemispherical bowl in a Stokes approximation, J. Phys. Conf. Ser. 1683 (2) (2020) 022076.
[35] A. Kharicha, I. Teplyakov, Y. Ivochkin, M. Wu, A. Ludwig, A. Guseva, Experimental and numerical analysis of free surface deformation in an electrically driven flow, Exp. Therm. Fluid Sci. 62 (2015) 192–201.
[36] I. Teplyakov, D. Vinogradov, Y. Ivochkin, Experimental study of the velocity of the electrovortex flow of In-Ga-Sn in hemispherical geometry, Metals 11 (11) (2021) 1806.
[37] D.A. Vinogradov, Y.P. Ivochkin, I.O Teplyakov, Investigation of the Taylor vortices in electrovortex flow, J. Phys. Conf. Ser. 891 (1) (2017) 012059.
[38] A. Kharicha, M. Al-Nasser, H. Barati, E. Karimi-Sibaki, A. Vakhrushev, M. Abdi, et al., Tornados and cyclones driven by Magneto-hydrodynamic forces, Eur. J. Mech. B/Fluids 94 (2022) 90–105, https://doi.org/10.1016/j.euromechflu.2022.02.001. Available from.
[39] E. Karimi-Sibaki, A. Kharicha, M. Abdi, A. Vakhrushev, M. Wu, A. Ludwig, et al., A numerical study on the influence of an axial magnetic field (AMF) on vacuum arc remelting (VAR) process, Metall. Mater. Trans. B 52 (5) (2021) 3354–3362.
[40] Y. Plevachuk, V. Sklyarchuk, S. Eckert, G. Gerbeth, R. Novakovic, Thermophysical properties of the liquid Ga-In-Sn eutectic alloy, J. Chem. Eng. Data 59 (3) (2014) 757–763.
[41] D.A. Vinogradov, I.O. Teplyakov, Y.P. Ivochkin, A. Kharicha, On the applicability of the electrodynamic approximation in the simulation of the electrovortex flow in the presence of an external magnetic field, in: Journal of Physics: Conference Series, Institute of Physics Publishing, 2018.
[42] Ansys® Fluent, 14.5, Help System, ANSYS, Inc. Ansys® Fluent, 14.5, help system, ANSYS, Inc.
[43] D.A. Vinogradov, Y.P. Ivochkin, I.O. Teplyakov, Effect of the Earth's Magnetic Field on the Electric-Vortex-Flow Structure, Dokl. Phys. 63 (2018) 447–450, https://doi.org/10.1134/S1028335818110046.